Revista Mexicana de Astronomía y Astrofísica, **41**, 45–55 (2005)

3D SIMULATIONS OF THE FRAGMENTATION OF PHOTOEVAPORATING CLUMPS EMBEDDED IN A STELLAR WIND

A. C. Raga,[1] W. Steffen,[2], and R. F. González[1]

Received 2004 October 7; accepted 2004 November 10

RESUMEN

Presentamos simulaciones numéricas tridimensionales de la interacción de un núcleo neutro con un viento y un campo radiativo ionizante externos. Encontramos que modelos con campos radiativos débiles llevan a la fragmentación del núcleo neutro a medida que éste evoluciona en el tiempo, lo cual está de acuerdo con modelos previos de la interacción de un núcleo denso con un viento. Modelos con campos radiativos ionizantes más fuertes tienen como resultado menos fragmentación, y para campos radiativos suficientemente fuertes sólo se produce una condensación densa.

ABSTRACT

We present 3D numerical simulations of the interaction of a dense, neutral clump with an impinging external wind+ionizing photon field. We find that models with very weak ionizing photon fields produce clumps that fragment as the time evolution proceeds, in agreement with previous clump/wind interaction models. Models with stronger ionizing photon fields present less fragmentation, and for strong enough photon fields only a single, dense condensation is produced.

Key Words: **ISM: H II REGIONS — ISM: KINEMATICS AND DYNAMICS — ISM: PLANETARY NEBULAE**

1. INTRODUCTION

Two related problems have received substantial attention in the past:

- The interaction of neutral clumps with an impinging wind.
- The photoevaporation of neutral clumps by an impinging ionizing photon field.

The first of these problems has been studied analytically by a number of authors among which we find Schwartz (1978), Blandford & Königl (1979), and Klein, McKee, & Collela (1994). In addition to analytical calculations, the following authors have performed numerical hydrodynamical simulations of the problem, each with emphasis on different astrophysical contexts: Różyczka & Tenorio-Tagle (1987); Klein, McKee, & Colella (1994); Raga et al. (1998), and Steffen & López (2004).

The problem of photoevaporated clumps was studied analytically by Dyson (1968), Bertoldi (1989), Bertoldi & McKee (1990), Pastor, Cantó, & Rodríguez (1991), and Henney & Arthur (1998). Numerical simulations of this problem were carried out by Lefloch & Lazareff (1994) and Mellema et al. (1998).

The combined interaction of a neutral structure with an impinging wind+ionizing photon flux was studied analytically by Henney et al. (1996). These authors noted the existence of two regimes:

- a "high ionizing photon flux" regime in which a strong photoevaporated wind interacts with the external, impinging, wind through the formation of a detached, two-shock structure,
- a "low ionizing photon flux" regime in which the impinging wind confines the photoevaporated material to a thin shell surrounding the neutral structure.

These ideas were extended to the case of the photoevaporation of a stratified, neutral clump by Arthur & Lizano (1997). Numerical simulations of this problem have been carried out (García-Arredondo, Henney, & Arthur 2001), but only for flows in the "high ionizing photon flux" regime.

[1]Instituto de Ciencias Nucleares, Universidad Nacional Autónoma de México, México, D. F., México.

[2]Instituto de Astronomía, Universidad Nacional Autónoma de México, Ensenada, B. C., México.

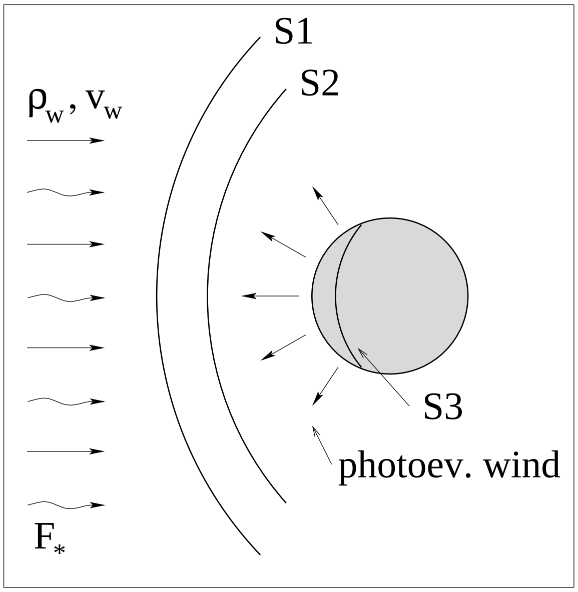

Fig. 1. Schematic diagram showing a neutral clump interacting with an impinging, plane-parallel wind (of density ρ_w and velocity v_w) and an ionizing photon flux F_*. For large enough values of F_*, a photoevaporated wind leaves the clump and interacts with the external wind, forming a detached, two-shock structure (shocks S1 and S2). For lower values of F_*, a confined photoevaporated clump region will form, shock S2 will be absent, and shock S1 will lie close to the surface of the clump. The high-pressure, photoevaporated clump region drives a third shock (S3) into the clump. This shock eventually goes through the clump, compressing the neutral clump material and setting it into motion.

In the present paper we study the transition between the "low ionizing photon flux" and the "high ionizing photon flux" regimes with a series of 3D numerical simulations (which include a gasdynamical description as well as the transfer of ionizing photons). With these simulations we obtain a qualitative description of the flows, and study the fragmentation of the clumps for flows in both regimes.

The paper is organized as follows. In §2, we discuss the analytic clump/wind+ionizing photon field model of Henney et al. (1996), and derive the equations which are necessary for choosing sets of parameters that produce flows in the two regimes (described above). In §3, we describe the model parameters, and present the results obtained from the numerical simulations. In §4, we present a more detailed discussion of the clump fragmentation that occurs in the different models. Finally, the results are summarized in §5.

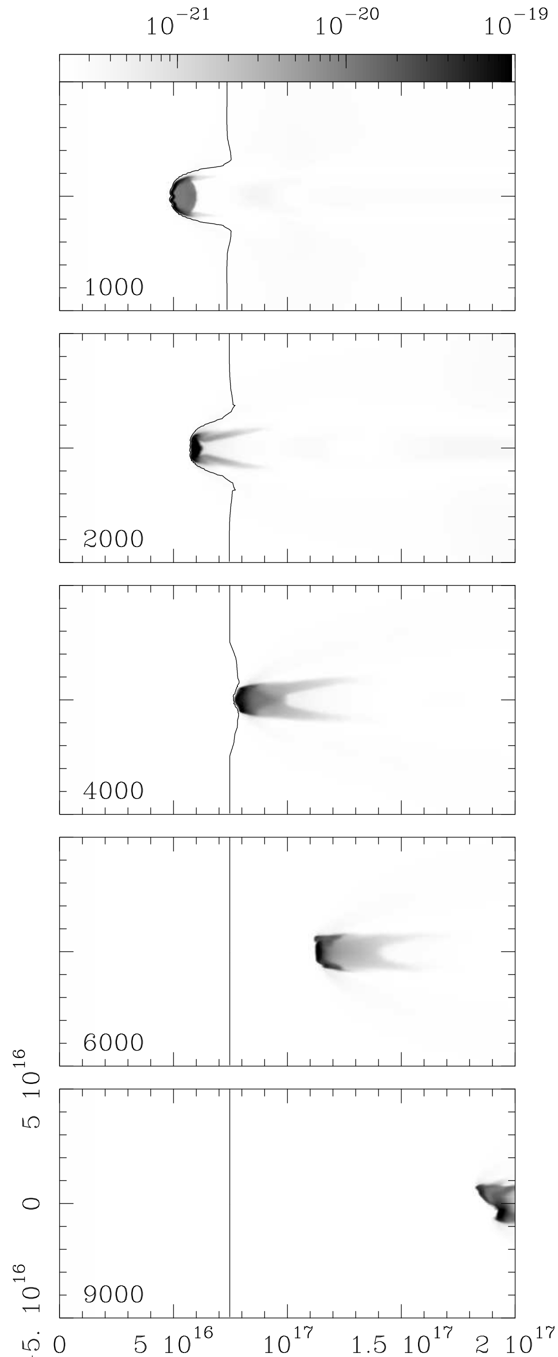

Fig. 2. Results obtained from model M1. Time-sequence of the density stratification on the xz-plane which passes through the center of the initial clump. The density stratifications are depicted with the logarithmic greyscale given (in g cm^{-3}) by the bar on the top. The single contour corresponds to a hydrogen ionization fraction of 0.5, with the material to the left being more highly ionized. The five frames which are shown correspond to the integration times (in years) given by the label on the bottom left of each frame. The x- and y- axes are labeled in cm, with the initial position of the center of the clump on the plane being $x_0 = 5 \times 10^{16}$ cm and $y_0 = 0$.

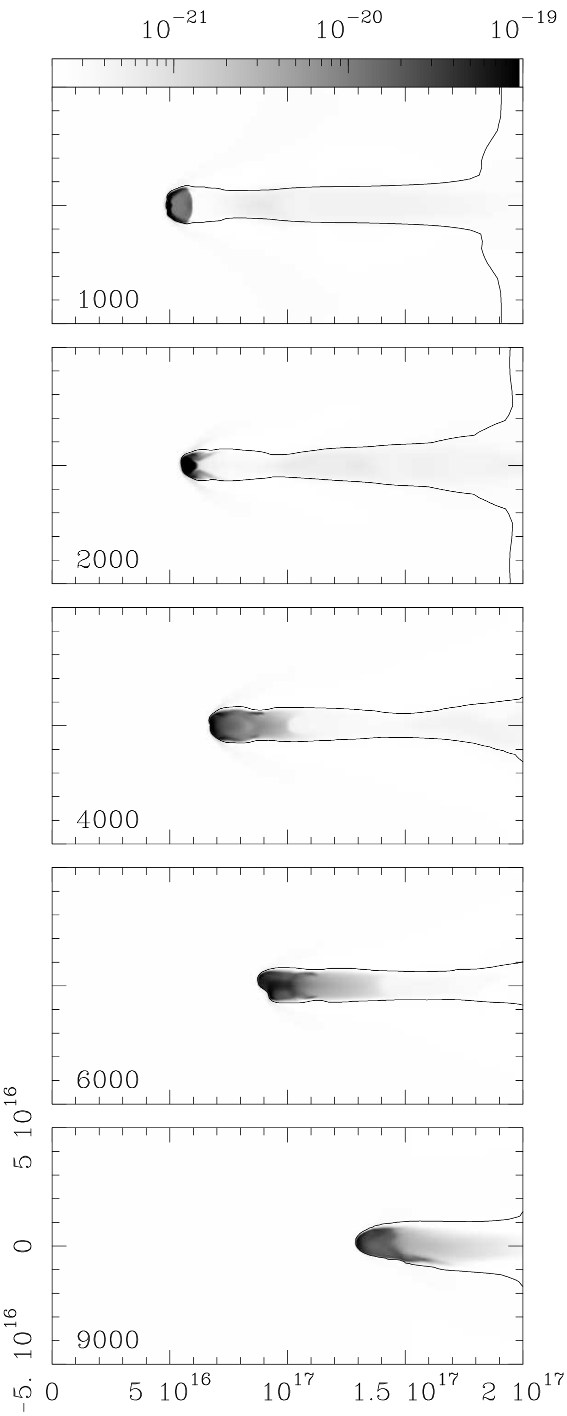

Fig. 3. The same as Fig. 2, but for model M2.

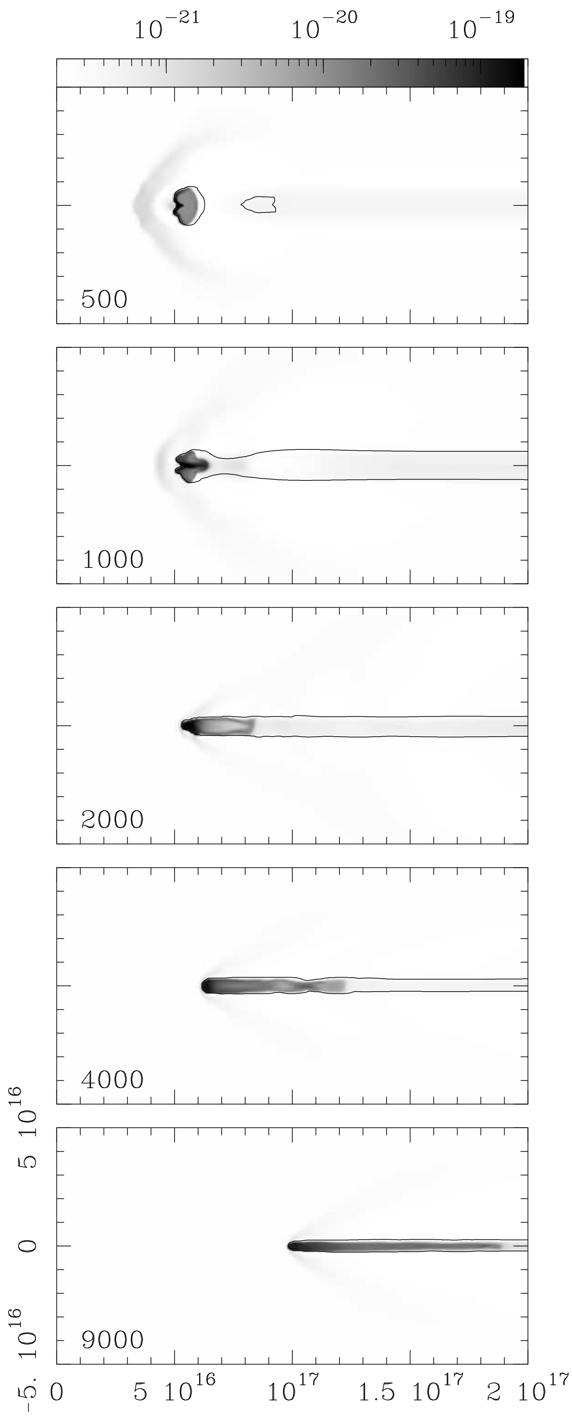

Fig. 4. The same as Fig. 2, but for model M3.

2. GENERAL CONSIDERATIONS

Let us consider a dense clump of radius r_c which interacts with an ionizing photon flux (with a number of photons F_* per unit area and time) and a wind (of density ρ_w and velocity v_w) which impinges on the clump from the same direction. The source of both the ionizing photons and the wind is assumed to be at a distance $D \gg r_0$. This situation is shown in a schematic way in Figure 1.

This situation is found for the interaction of a clump with the ionizing photon field from the exciting stellar source of an H II region and with the expanding H II region which flows past the clump. A similar dynamic situation is found for clumps em-

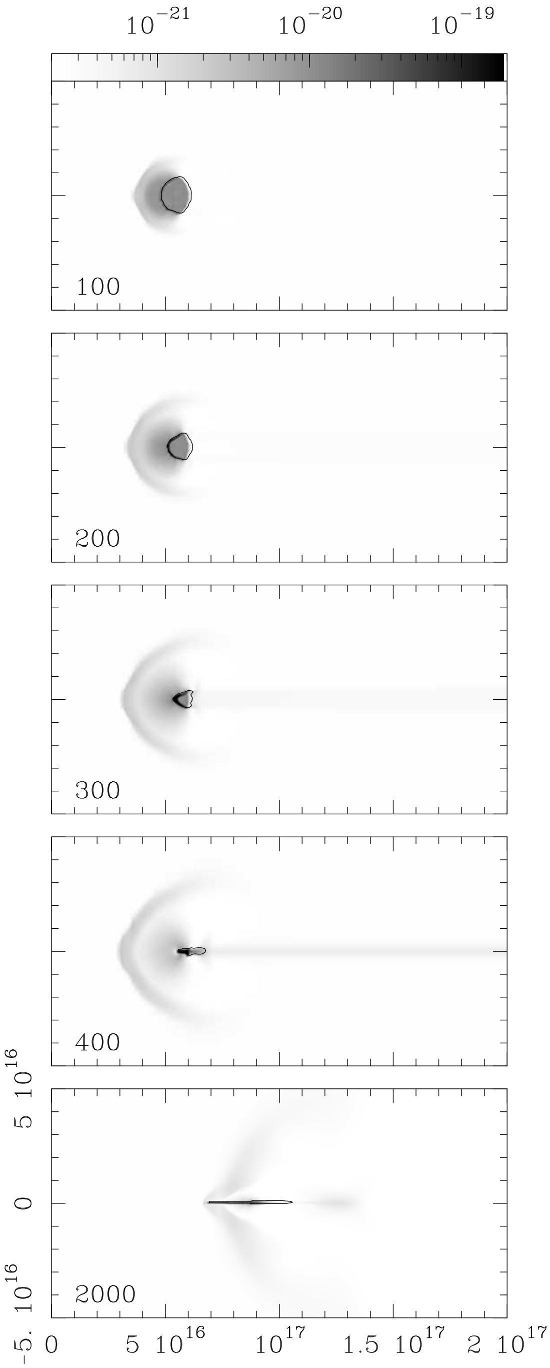

Fig. 5. The same as Fig. 2, but for model M4.

bedded within the wind ejected by an O star.

This kind of interaction was studied in the context of the Orion proplyds by Henney et al. (1996). Here, we give a brief description of some of the analytic results obtained by these authors.

For the case of a clump embedded in a low pressure medium, it has been shown that an impinging ionizing photon flux drives a D-critical ionization front into the clump (Dyson 1968). This ionization front produces a photoevaporated flow that leaves from the surface of the clump at a velocity c_I equal to the sound speed of the photoionized gas (i.e., $c_I \approx 10$ km s^{-1}), as shown in Fig. 1.

This photoevaporated flow has a density stratification which approximately follows a law:

$$n(r) = n_0 \left(\frac{r_0}{r}\right)^2 , \qquad (1)$$

where n is the number density, r the spherical radius and r_0 the radius of the ionization front (which initially lies on the surface of the clump, so that initially we have $r_0 = r_c$). This equation has been derived on the assumption that the photoevaporated wind has a spherical divergence and a constant velocity c_I (Henney et al. 1996 studied the modifications to this equation resulting from the outwards acceleration of this wind which follows from the isothermal Bernoulli's theorem).

The density n_0 at the base of the photoevaporated wind is related to the ionizing photon flux F_0 impinging on the surface of the clump through:

$$F_0 = n_0 c_I \, . \qquad (2)$$

The remaining equation for determining the on-axis structure of the photoevaporated wind is:

$$F_* = F_0 + \int_{r_0}^{\infty} n^2(r)\alpha \, dr = F_0 + F_0^2 \frac{r_0 \alpha}{3c_I^2} , \qquad (3)$$

where $F_* = S_*/4\pi D^2$ (with S_* being the ionizing photon production rate, and D the distance to the star) is the number of photons per unit area and time arriving from the star and α ($\approx \alpha_B \approx 2.6 \times 10^{-13}$ cm^3 s^{-1}) is the H recombination coefficient. The first equality of this equation simply states that along the symmetry axis of the problem (see Fig. 1), the photon flux F_0 arriving at the surface of the clump plus the number of recombinations (per unit area and time) within the photoevaporated wind is equal to the number of photons arriving from the star.

In calculating the number of recombinations, we have carried out the integral of the recombinations per unit volume from the radius r_0 of the recombination front out to infinity (see the first equality of Eq. 3). In reality, for a stationary, photoevaporated wind this integral should extend only out to a distance D (i.e., the distance from the clump to the photon source), and in a real flow the photoevaporated wind probably has not evolved for a long enough time and actually only travels out from the clump to a much shorter distance. However, for the $1/r^2$ density law of the photoevaporated wind (see Eq. 1), the recombination integral (see the first equality of Eq. 3) is dominated by the contribution from the region with $r < 2r_0$, so that one actually can extend the integration out to infinity without introducing large errors.

The integral in Eq. (3) can be carried out by assuming that the wind is isothermal (so that the recombination coefficient α can be taken out of the integral), and using Eq. (1). The second equality of Eq. (3) was obtained in this way, also eliminating n_0 in favor of F_0 using Eq. (2).

Equation (3) is then a quadratic equation relating F_0 with F_*, which can be inverted to give:

$$F_0 = \frac{F_c}{2}\left[\sqrt{1+4F_*/F_c}-1\right], \tag{4}$$

with

$$F_c \equiv \frac{3\,c_I^2}{r_0\alpha}. \tag{5}$$

The simple model described above gives a complete description of the photoevaporated wind. If we have a photon flux F_* impinging on the "clump+photoevaporated wind" system, we can use Eq. (4) to determine the flux F_0 actually reaching the surface of the clump (F_0 depending both on F_* and the radius r_0 of the ionization front, see Eq. 5). Equations (1) and (2) then give us the density stratification $n(r)$ in the photoevaporated wind, which is assumed to have a constant velocity c_I as it flows away from the neutral clump.

This photoevaporated wind then interacts with the external, impinging wind (which is shown in Fig. 1, and has a constant velocity v_w and number density $n_w = \rho_w/m$, where m is the average mass per atom or ion). The interaction of the two winds leads to a two-shock structure (see Fig. 1). The on-axis distance r_w of this structure from the center of the clump is determined by the ram pressure balance condition:

$$n_w v_w^2 = n(r_w)c_I^2, \tag{6}$$

which can be combined with Eqs. (1 to 2) to obtain

$$r_w = \lambda^{1/2} r_0, \tag{7}$$

where

$$\lambda \equiv \frac{F_0 c_I}{n_w v_w^2}. \tag{8}$$

Henney et al. (1996) argued that for $\lambda > 1$, a situation similar to the one shown in our Fig. 1 is obtained, with a detached photoevaporated wind/impinging external wind two-shock structure.

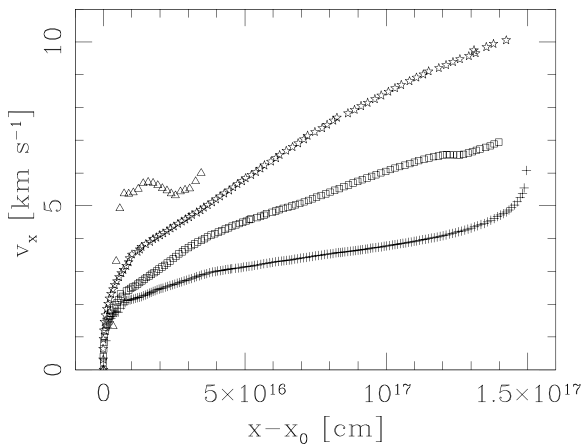

Fig. 6. Density weighted, mean velocity of the neutral clump material (the x-component of this velocity being shown, as the other two components are very small) as a function of center of mass position. The results for model M1 (stars, curve that ends on the upper right), model M2 (squares, curve that follows the one of M1 but at lower velocities), M3 (crosses, lower velocity curve) and M4 (triangles, curve, that ends at lower x values) are shown. The position of the center of mass is given with respect to the initial position of the clump.

For the case where $\lambda < 1$ (in which Eq. 7 gives an erroneous $r_w < r_0$), the photoevaporated cloud material will no longer be able to form a free-flowing photoevaporated wind, and instead a confined region of photoionized clump material will form. This region will be limited by the ionization front and by the post-bow shock impinging wind material. In this flow configuration, the S2 shock of Fig. 1 (in which the photoionized wind is shocked) will be absent.

In the present paper, we compute four models of the interaction of a neutral clump with an impinging wind+photoionizing photon flux, chosen so as to span a range of the dimensionless parameter λ. These models are described in the following section.

3. NUMERICAL SIMULATIONS

In this section we present 3D numerical simulations computed with the adaptive grid "yguazú-a" code (described in detail by Raga, Navarro-González, & Villagrán-Muniz 2000). The version of the code which we use solves the gasdynamic equations, a rate equation for neutral/ionized hydrogen, and the radiative transfer of the direct photons at the Lyman limit (the diffuse ionizing photon field being considered only by using the case B recombination coefficient). A parametrized cooling function (which depends on the density, the temperature and the hydrogen ionization fraction) and a photoionization heating term are included in the energy equa-

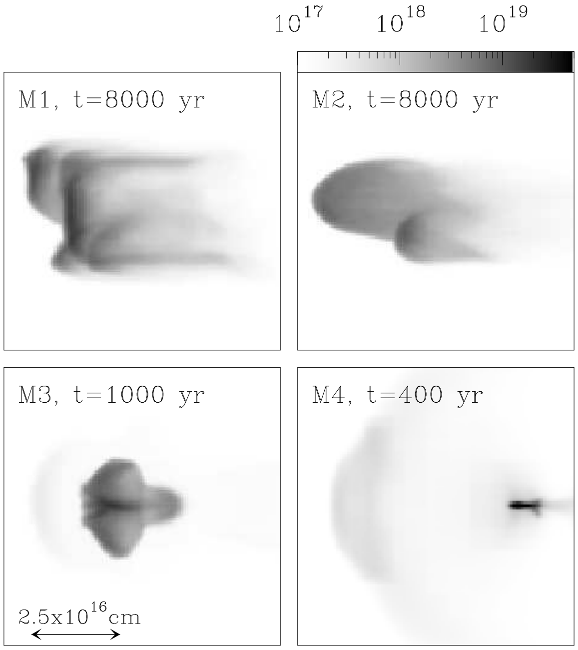

Fig. 7. Column density (integrated along the y-axis) for selected time frames of models M1, M2, M3, and M4. The four plots are labeled with the corresponding models and integration times. The column densities are depicted with the logarithmic greyscale given (in cm^{-2}) by the bar on the top right. Only a small region of the computational domain, centered on the clump, is shown, and the spatial scale of the plots is given by the arrow on the bottom left.

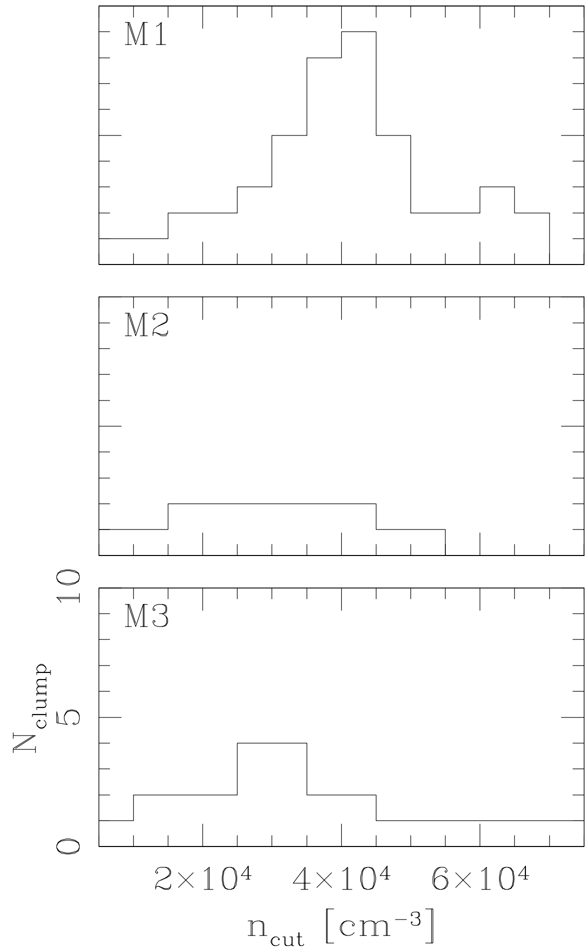

Fig. 8. Number of clumps as a function of cutoff density n_{cut} calculated with the 3D density stratifications of the $t = 8000$ yr time frame of model M1 (top), the $t = 8000$ yr frame of model M2 (center) and the $t = 1000$ yr of model M3 (bottom).

tion. This version of the yguazú-a code is described in detail by Raga & Reipurth (2004).

We have computed four models of the interaction of a neutral clump with an impinging external wind+ionizing photon flux. For the four models we have assumed that we have plane-parallel, uniform, fully ionized wind entering the computational domain at $x = 0$, with a density $n_w = 100$ cm^{-3}, temperature $T_w = 10^4$ K and velocity $v_w = 30$ km s^{-1}. The characteristics of this wind are representative of the properties of an expanding H II region.

In all models we have considered a spherical, isothermal, neutral clump of initial temperature $T_c = 100$ K, outer radius $r_c = 10^{16}$ cm, with a nonuniform density

$$n_c(x,y,z) = < n_c > + \eta \sin\left[\frac{2\pi(x-x_0)}{L}\right] + \eta \sin\left[\frac{2\pi(y-y_0)}{L}\right] + \eta \sin\left[\frac{2\pi(z-z_0)}{L}\right] , \qquad (9)$$

with $< n_c > = 5000$ cm^{-3}, $L = r_0/4$, and $\eta = 0.1$, and where (x_0, y_0, z_0) is the position of the center of the clump. This small amplitude clump density variability was imposed in order to break the axisymmetry of the problem, and allow the formation of non-axisymmetric, 3D structures in the evolution of the flow.

The four models (models M1 through M4) differ in the magnitude of the impinging ionizing photon flux. In model M4, the ionizing photon flux impinging at the $x = 0$ boundary of the computational grid has a value $F_*(M4) = F_{*,0} = 3.98 \times 10^{10}$ cm^{-2} s^{-1}, which corresponds to a source emitting $S_* = 5 \times 10^{47}$ s^{-1} ionizing photons per unit time at a distance $D = 10^{18}$ cm. The other models have different values of F_*, which are listed in Table 1. In all models, the spectrum of the source is assumed to have a black-body temperature $T_* = 50,000$ K (this

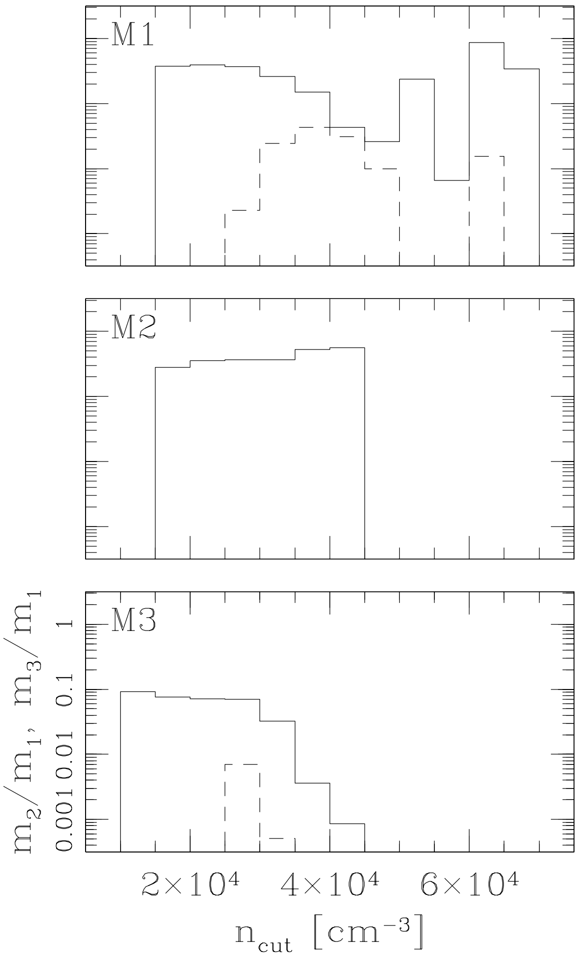

Fig. 9. Ratio m_2/m_1 (between the mass of the second most massive and that of the most massive condensation, solid line) and the ratio m_3/m_1 (between the mass of the third most massive and that of the most massive condensation, dashed line) as a function of cutoff density n_{cut} calculated for the $t = 8000$ yr time frame of model M1 (top), the $t = 8000$ yr frame of model M2 (center) and the $t = 1000$ yr frame of model M3 (bottom).

temperature entering only into the calculation of the heating due to photoionization, see Raga & Reipurth 2004).

With the values of F_* and r_c ($= 10^{16}$ cm for all models, see above) we can calculate the value F_0 of the ionizing flux impinging on the surface of the clump, using Eqs. (4–5), setting $r_0 = r_c$ (which is valid for the initial stages of the clump evolution, see §2). The resulting values of F_0 are listed in Table 1. These F_0 values give the ionizing photon fluxes arriving at the surface of the clump at times in which the photoevaporated wind has formed and propagated to a distance of at least $\sim 2r_c$ (measured from the center of the clump), so that the integral of Eq. (3), which extends to infinity, gives a value similar to the recombinations in the spatially limited photoevaporated wind of the numerical models.

TABLE 1

CLUMP MODELS[a]

Model	F_* $[F_{*,0}]$[b]	F_0/F_*[c]	λ[d]
M1	10^{-4}	0.997	4.42×10^{-3}
M2	10^{-2}	0.787	0.35
M3	10^{-1}	0.413	1.82
M4	1	0.156	6.90

[a]Parameters of the models described in section 3.

[b]The ionizing photon fluxes impinging on the computational grid are given in units of $F_{*,0} = 3.98 \times 10^{10}$ cm^{-2} s^{-1}.

[c]Fraction of the impinging ionizing photon flux actually arriving at the surface of the clump.

[d]Dimensionless parameter determining the ram pressure balance between the impinging wind and the photoionized flow (see Eq. 8).

With these values of F_0 we can calculate the dimensionless parameter λ (see Eqs. 7–8) which determines whether or not an initially free-flowing, photoevaporated wind is formed. The values of λ given in Table 1 show that our four models span a range from $\lambda = 6.9$ down to $\lambda \approx 4 \times 10^{-3}$ with two models (M1 and M2) with $\lambda < 1$ and two models (M3 and M4) with $\lambda > 1$. We should note that the values of F_0 and λ for models M1 and M2 do not have a clear physical meaning, since the analytic model with which they have been calculated (see §2) only applies for $\lambda > 1$.

All of the models were computed on a 6-level, binary adaptive grid with a maximum resolution of 3.9×10^{14} cm (so that the initial diameter of the clump is resolved with ~ 50 grid points at the highest grid resolution). The computational domain has a spatial extent of 2×10^{17} cm along the x-axis, and of 10^{17} cm along the y- and z-axes. The clump is initially centered in the middle of the yz-extension of the grid, and it is placed at $x_0 = 5 \times 10^{16}$ cm from the left boundary of the x-axis. In this boundary we impose the inflow condition for the impinging wind (which enters the domain with a velocity parallel to the x-axis), as well as the flux F_* of impinging ionizing photons (which also propagate parallel to the x-axis). We apply a free outflow condition on all of the other grid boundaries. With this configuration, we have then carried out time-integrations with a Δt=100 yr interval between successive outputs.

Figures 2 to 5 show time-sequences of a few of the density stratifications obtained from models M1-M4, respectively. These graphs show logarithmic greyscale depictions of the density stratification in an xy-plane which goes through the center of the initial clump, and also show a single contour line corresponding to a 50% hydrogen ionization fraction (on the same plane).

From Fig. 2, we see that for model M1 only the region with $x < 7.5 \times 10^{16}$ cm has an ionization fraction $> 50\%$. This is due to the fact that the very low ionizing photon flux of this model can only photoionize a column of wind material (with a $n_w = 100$ cm^{-3} density, see above) with a spatial extent $D_S = F_*/(n_w^2\,\alpha) \sim 1.5 \times 10^{15}$ cm (also see Table 1). Therefore, in our model M1 simulation the initially ionized, impinging wind enters the computational grid and rapidly starts to recombine, forming an extended recombination region as it flows along the x-axis. In Fig. 3, we see that for model M2 most of the computational domain (except for the regions shaded by the neutral clump material and the far right of the domain for the $t = 1000$ and 2000 yr frames) has an ionization fraction $> 50\%$. This is to be expected as the impinging ionizing photon flux of model M2 (see Table 1) is able to photoionize a column of material of density $n_w = 100$ cm^{-3} with a spatial extent $D_S \approx 1.5 \times 10^{17}$ cm, which is close to the x-extent of the computational grid. Figs. 4 and 5 show that for models M3 and M4 (respectively) the only regions with ionization fractions lower than 50% are the ones shaded by the neutral clump material.

Figures 2 to 5 show that the time evolutions of the different models are quite different. In model M4 (Fig. 5), the cloud rapidly colapses to a single, axially elongated feature, with strongly decreasing mass as a function of time. For this model, by a $t = 2400$ yr integration time all of the initial clump material has been photoionized (note that we have studied the flow stratifications only at 100 yr intervals, see above). In model M3, by the time that the clump starts to leave the computational domain (at $t \approx 15{,}000$ yr), it has a neutral mass of only 7% of the initial cloud mass. In model M2, the neutral clump starts to leave the computational grid at $t \approx 10{,}000$ yr, and at that time it has a neutral mass of 57% of the initial cloud mass. In model M1, the clump starts to leave the computational domain at $t = 9000$ yr, and at that time has a neutral mass of 99% of the initial mass of the neutral cloud.

In the early frames of Figure 2 to 5, it is evident that while in models M1 and M2 (Figs. 2 and 3) the impinging wind forms a bow shock around the dense clump, models M3 and M4 (Figs. 4 and 5) have a photevaporated clump wind which shocks against the impinging wind in a detached, two-shock structure. This is in agreement with the expectation that for $\lambda > 1$ (i. e., for models M3 and M4, see Table 1), a detached two-shock structure should be formed (see §2).

Figure 6 shows the average flow velocity of the neutral clump material (i.e., the part of the material belonging to the initial cloud which still remains neutral) as a function of the position of the barycenter of this material. As time evolves, the barycenter of the neutral clump material moves along the x-axis to the right of the the central position of the initial clump. Also, as the material is pushed along (by the rocket effect and/or by the impinging wind), its velocity increases. From Fig. 6, we see that in model M4 the neutral clump rapidly accelerates to a velocity of $\approx$ 5-6 km s^{-1} and then remains at this velocity until it is fully photoevaporated when it reaches a distance of $\approx 3 \times 10^{16}$ cm (measured from the position x_0 of the center of the initial clump). In model M3, the neutral clump has lower velocities of 2–3 km s^{-1}, only reaching velocities of $\approx$ 6 km s^{-1} shortly before it leaves the computational grid (which is just before it becomes fully ionized). The neutral clump of model M2 shows systematically higher velocities as a function of position. Finally, in model M1 the neutral clump is accelerated to the highest velocity (of $\approx$ 10 km s^{-1}) obtained from our four models.

4. CLUMP FRAGMENTATION

In this section we discuss the fragmentation of the initial neutral cloud as a result of its interaction with the impinging wind and ionizing photon flux. From Figs. 2 to 3, it is clear that models M1 and M2 towards their later evolutionary stages develop a complex density structure with more than one "condensation". On the other hand, models M3 and M4 (see Figs. 4 to 5) rapidly collapse to form a single, filamentary structure aligned with the x-axis.

At relatively early stages, just as the clump is collapsing, model M3 does develop a short-lived, morphologically more complex structure (see the $t = 1000$ yr frame of Fig. 4). We do not see a similar evolutionary stage for model M4, but this is probably the result of an inappropriate time-resolution in the outputs that we are analizing (which are taken at 100 yr intervals, see above).

In order to illustrate the condensation structure formed in our models, in Figure 7 we show the column densities obtained by integrating the number density along the y-axis for "late", $t = 8000$ yr evolutionary states of models M1 and M2, for $t = 1000$ yr for model M3 (just as the clump is collapsing), and for $t = 400$ yr for model M4 (just after the collapse). From Fig. 7, it is clear that at the later evolutionary states, model M1 produces a system of several condensations, while model M2 appears to produce only two condensations. Model M3 produces an "umbrella-shaped" structure which might be divided into more than one condensation. Finally, as stated above, we never see multiple condensations in the rapidly evolving model M4.

In order to quantify the properties of the 3D condensation structures produced by models M1, M2, and M3, we have analyzed the $t = 8000$ yr frames of models M1 and M2 and the $t = 1000$ yr frame of model M3 (see Fig. 6) in the following way. We first introduce a density cutoff value n_{cut}, and then find the contiguous density structures with densities $n > n_{cut}$. We then calculate the number of condensations (as well as the mass of each of these condensations) as a function of the cutoff density n_{cut}, with n_{cut} varying from 5×10^3 cm^{-3} to 7×10^4 cm^{-3} in intervals of 5×10^3 cm^{-3}. Finally, we reject all of the condensations which have density differences of less than 10^4 cm^{-3} between their peak density and the valleys separating them from the other condensations (this is done in order to consider only condensations with relatively high peaks with respect to their surroundings).

The results of this process are shown in Figures 8 and 9. Fig. 8 shows the number of condensations as a function of cutoff density n_{cut}. In all models, for low enough cutoff densities all of the clump is seen as a single condensation. For values of n_{cut} larger than the maximum density found in the simulation, the algorithm detects no clumps. We can appreciate this high density cutoff in the N_{clump} vs. n_{cut} graphs for models M1 and M2, but not for the one of model M3, which has a maximum number density of 7.6×10^4 cm^{-3}. From Fig. 8, it is clear that while model M1 shows a number of condensations (the value of this number depending on the value of n_{cut}), model M2 shows only two condensations (and only for appropriate values of n_{cut}). Model M3 shows 4 condensations for $n_{cut} = 25{,}000$ or 30,000 cm^{-3}.

In order to give an idea of the mass distribution of the condensations, in Figure 9 we plot the m_2/m_1 and m_3/m_1 ratios as a function of n_{cut}, where m_1 is the mass of the most massive condensation (determined as a contiguous region of density greater than n_{cut}, see above), m_2 is the mass of the second and m_3 of the third most massive condensation. From this figure, we see that for models M1 and M2, the m_2/m_1 ratio is of order 1 for most values of n_{cut}. For model M1, the m_3/m_1 ratio is $\sim 0.01 - 0.06$ (this ratio cannot be calculated for model M2, as our algorithm only finds two condensations for this model, see Fig. 8), and we also find that the remaining, lower mass condensations have masses of the same order as m_3.

Therefore, models M1 and M2 produce two condensations with masses of similar order of magnitude, and model M1 additionally produces a few other very low mass condensations (with masses of a few percent of the total mass of the neutral clump). These smaller condensations are not present in model M2, probably indicating that the ionizing photon field of model M2 fully photoevaporates low mass condensations which are formed as a result of the clump/impinging wind interaction. From Fig. 9, we see that in model M3 most of the neutral clump is concentrated in a single condensation, with the second condensation having only $\sim 10\%$ of the clump mass.

We can summarize these results as follows:

- the clumps of our two models with $\lambda < 1$ (models M1 and M2) fragment as the time-integration proceeds,
- model M1 produces a spectrum of condensations, with masses covering a range of approximately two orders of magnitude, and two massive condensations with masses of the order of $\sim 1/2$ of the total neutral mass,
- model M2 produces two condensations with properties similar to the ones of the most massive condensations of model M1, but in this model the lower density condensations are absent,
- the clumps of our models with $\lambda > 1$ (models M3 and M4) collapse into a filamentary structure aligned with the x-axis, and do not show a structure of condensations,
- for a short time, during the collapse of the clump, model M3 shows a short-lived condensation structure, with most of the mass concentrated in a single condensation.

5. CONCLUSIONS

We have presented 3D numerical simulations of the interaction of a neutral clump with an impinging wind+ionizing photon flux. This problem is relevant for modelling neutral knots immersed in an expanding H II region or in a planetary nebula. We have presented four models, with identical parameters except for the impinging ionizing flux, whose value spans four orders of magnitude (see Table 1). These models could actually apply to neutral clumps within a single photoionized nebula, the higher ionizing flux models corresponding to clumps close to the exciting star(s) and the ones with lower flux corresponding to clumps close to or within the ionization front at the outer edge of the nebula.

We find that the models with strong ionizing photon fluxes (models M3 and M4, see Figs. 4 and 5) produce a photoevaporated wind which interacts with the external wind in a detached, two-shock structure. In these models, the impinging wind does not interact directly with the surface of the clump, and the clump evolves as if the external wind were not present (see, e.g., the numerical simulations of Mellema et al. 1998). In the models with lower ionizing photon fluxes (models M1 and M2, see Figs. 2 and 3), the wind does interact directly with the surface of the neutral clump (see, e.g., the numerical simulations of Raga et al. 1998). Even though we have imposed an initially perturbed density structure for the clump (see Eq. 9), models M3 and M4 result in the formation of a strong, axial feature (although model M3 produces a short-lived structure of several condensations, see Fig. 8 and §4). On the other hand, models M1 and M2 produce a clear fragmentation of the clump towards later evolutionary times. Model M1 (with basically zero ionizing photon flux) produces two large condensations (each one with a substantial fraction of the neutral clump mass) and a number of smaller ones (see Figs. 8 and 9). Model M2 (with a larger ionizing photon flux, see Table 1) produces only two large condensations, the smaller ones being destroyed by the impinging ionizing photon flux (see Figs. 8 and 9).

From this, we conclude that while the interaction of a dense clump with an impinging wind leads to the fragmentation of the clump, the presence of an ionizing photon flux reduces this fragmentation. This reduction of fragmentation occurs in two ways:

- the presence of a low ionizing radiative field (such that one has a dimensionless parameter $\lambda < 1$, but of order one, as in model M2 of Table 1) results in the photoevaporation of the smaller fragments, narrowing the size spectrum of the fragmentation process,

- the presence of a high ionizing radiative field (such that $\lambda > 1$, see models M3 and M4 in Table 1) produces a photoevaporated wind which stops the impinging, external wind from interacting directly with the clump. In this case, the clump is compressed into a single, elongated, high-density structure by the high pressure of the photoevaporated material.

The details of the fragmentation process will of course depend on the spatial resolution of the numerical simulations, but the qualitative effects of the presence of an ionizing photon field are probably well described by our present simulations.

To some extent, these results appear to go against observations of strongly fragmented clumps within H II regions. An example of this are Thackeray's globules (see, e.g., Reipurth, Raga, & Heathcote 2003), which are a group of photoevaporating clumps with a wide spectrum of sizes and masses. In our models, such structures could only be obtained for a short period, at the times at which the initial clump is collapsing to form the elongated, axial structure.

An additional ingredient, which is absent in our models, is the possible existence of strong density inhomogeneities in the initial neutral structure. Our present study is limited to simulations of clumps with small inhomogeneities in their initial density structures (see Eq. 9), introduced only to break the axisymmetry of the problem. In reality, much stronger inhomogeneities might be present, which might lead to a stronger and longer-lasting fragmentation of the neutral structures. We will study this problem in a forthcoming paper.

This work was supported by the CONACyT grants 36572-E, 41320-F and 43103-F and the DGAPA (UNAM) grants IN 112602 and IN 111803.

REFERENCES

Arthur, S. J., & Lizano, S. 1997, ApJ, 484, 810
Bertoldi, F. 1989, ApJ, 346, 735
Bertoldi, F., & McKee, C. F. 1990, ApJ, 354, 529
Blandford, R. D., & Königl, A. 1979, ApL, 20, 15
Dyson, J. E. 1968, Ap&SS, 1, 288
García-Arredondo, F., Henney, W., & Arthur, S. J. 2001, ApJ, 561, 830
Henney, W., & Arthur, S. J. 1998, AJ, 116, 322
Henney, W., Raga, A. C., Lizano, S., & Curiel, S. 1996, ApJ, 465, 216
Klein, R. I., McKee, C. F., & Collela, P. 1994, ApJ, 420, 213
Lefloch, B., & Lazareff, B. 1994, A&A, 289, 559
Mellema, G., Raga, A. C., Cantó, J., Lundqvist, P., Balick, B., Steffen, W., & Noriega-Crespo, A. 1998, A&A, 331, 335
Pastor, J., Cantó, J., & Rodríguez, L. F. 1991, A&A, 246, 551

Raga, A. C., Cantó, J., Curiel, S., & Taylor, S. 1998, MNRAS, 295, 738
Raga, A. C., Navarro-González, R., & Villagrán-Muniz, M. 2000, RevMexAA, 36, 67
Raga, A. C., & Reipurth, B. 2004, RevMexAA, 40, 15
Reipurth, B., Raga, A. C., & Heathcote, S. 2003, AJ, 126, 1925
Różyczka, M., & Tenorio-Tagle, G. 1987, A&A, 176, 329
Schwartz, R. D. 1978, ApJ, 223, 884
Steffen, W., & López, J. A. 2004, ApJ, 612, 319

Alejandro C. Raga and Ricardo F. González: Instituto de Ciencias Nucleares, UNAM, Apdo. Postal 70-543, 04510 México, D. F., México. (raga,ricardog@nuclecu.unam.mx).
Wolfgan Steffen: Instituto de Astronomía, UNAM, Apdo. Postal 877, 22800 Ensenada, B. C., México. (wsteffen@astrosen.unam.mx).